PROCEEDINGS OF THE ROYAL SOCIETY A MATHEMATICAL, PHYSICAL & ENGINEERING SCIENCES

Bifurcations with imperfect SO(2) symmetry and pinning of rotating waves

Francisco Marques, Alvaro Meseguer, Juan M. Lopez, J. Rafael Pacheco and Jose M. Lopez

Proc. R. Soc. A 2013 **469**, 20120348, published 13 February 2013

PROCEEDINGS OF THE ROYAL SOCIETY A

rspa.royalsocietypublishing.org

Research

Cite this article: Marques F, Meseguer A, Lopez JM, Pacheco JR, Lopez JM. 2013 Bifurcations with imperfect SO(2) symmetry and pinning of rotating waves. Proc R Soc A 469: 20120348.
http://dx.doi.org/10.1098/rspa.2012.0348

Received: 10 June 2012
Accepted: 17 January 2013

Subject Areas:
applied mathematics, fluid mechanics

Keywords:
equivariant Hopf bifurcation, imperfections, pinning phenomenon, Taylor–Couette flow, rotating Rayleigh–Benard convection

Author for correspondence:
Juan M. Lopez
e-mail: juan.m.lopez@asu.edu

Bifurcations with imperfect SO(2) symmetry and pinning of rotating waves

Francisco Marques[1], Alvaro Meseguer[1], Juan M. Lopez[2], J. Rafael Pacheco[2] and Jose M. Lopez[1]

[1]Departament de Física Aplicada, Universitat Politècnica de Catalunya, Girona Salgado s/n, Mòdul B4 Campus Nord, 08034 Barcelona, Spain
[2]School of Mathematical and Statistical Sciences, Arizona State University, Tempe, AZ 85287, USA

Rotating waves are periodic solutions in SO(2) equivariant dynamical systems. Their precession frequency changes with parameters and it may change sign, passing through zero. When this happens, the dynamical system is very sensitive to imperfections that break the SO(2) symmetry and the waves may become trapped by the imperfections, resulting in steady solutions that exist in a finite region in parameter space. This is the so-called pinning phenomenon. In this study, we analyse the breaking of the SO(2) symmetry in a dynamical system close to a Hopf bifurcation whose frequency changes sign along a curve in parameter space. The problem is very complex, as it involves the complete unfolding of high codimension. A detailed analysis of different types of imperfections indicates that a pinning region surrounded by infinite-period bifurcation curves appears in all cases. Complex bifurcational processes, strongly dependent on the specifics of the symmetry breaking, appear very close to the intersection of the Hopf bifurcation and the pinning region. Scaling laws of the pinning region width and partial breaking of SO(2) to Z_m are also considered. Previous as well as new experimental and numerical studies of pinned rotating waves are reviewed in the light of the new theoretical results.

1. Introduction

Dynamical systems theory plays an important role in many areas of mathematics and physics because it provides the building blocks that allow us to understand

the changes many physical systems experience in their dynamics when parameters are varied. These building blocks are the generic bifurcations (saddle–node, Hopf, etc.) that any arbitrary physical system experiences under parameter variation, regardless of the physical mechanisms underlying the dynamics. When one single parameter of the system under consideration is varied, codimension-one bifurcations are expected. If the system depends on more parameters, higher codimension bifurcations appear and they act as organizing centres of the dynamics.

The presence of symmetries changes the nature and type of bifurcations that a dynamical system may undergo. Symmetries play an important role in many idealized situations, where simplifying assumptions and the consideration of simple geometries result in dynamical systems equivariant under a certain symmetry group. Bifurcations with symmetry have been widely studied [1–6]. However, in any real system, the symmetries are only approximately fulfilled, and the breaking of the symmetries, owing to the presence of noise, imperfections and/or other phenomena, is always present. There are numerous studies of how imperfect symmetries lead to dynamics that are unexpected in the symmetric problem [7–12]. However, a complete theory is currently unavailable.

One observed consequence of imperfections in systems that support propagating waves is that the waves may become trapped by the imperfections [7,13–15]. In these various examples, the propagation direction is typically biased. However, a more recent experiment has considered a case of a rotating wave pinned by symmetry-breaking imperfections for parameter values near where its sense of precession changes sign [16]. We are unaware of any systematic analysis of the associated normal form dynamics for such a problem and this motivates the present study.

When a system is invariant to rotations about an axis (invariance under the SO(2) symmetry group), SO(2)-symmetry-breaking Hopf bifurcations result in rotating waves, consisting of a pattern that rotates about the symmetry axis at a given precession frequency without changing shape. This frequency is parameter dependent, and in many problems, when parameters are varied, the precession frequency changes sign along a curve in parameter space. What has been observed in different systems is that, in the presence of imperfections, the curve of zero frequency becomes a band of finite width in parameter space. Within this band, the rotating wave becomes a steady solution. This is the so-called pinning phenomenon. It can be understood as the attachment of the rotating pattern to some stationary imperfection of the system, so that the pattern becomes steady, as long as its frequency is small enough so that the imperfection is able to stop the rotation. This pinning phenomenon bears some resemblance to the frequency-locking phenomena, although in the frequency-locking case we are dealing with a system with two non-zero frequencies and their ratio becomes constant in a region of parameter space (a resonance horn), whereas here we are dealing with a single frequency crossing zero.

In this paper, we analyse the breaking of SO(2) symmetry in a dynamical system close to a Hopf bifurcation whose frequency changes sign along a curve in parameter space. The analysis shows that breaking SO(2) symmetry is much more complex than expected, resulting in a bifurcation of high codimension (about nine). Although it is not possible to analyse in detail such a complex and high-codimension bifurcation, we present here the analysis of five different ways to break SO(2) symmetry. This is carried out by introducing into the normal form all the possible terms, up to and including second order, that break the symmetry, and analysing each of these five terms separately. Three of these particular cases have already been analysed in completely different contexts unrelated to the pinning phenomenon [17–20]. In this study, we extract the common features that are associated with the pinning. In all cases, we find that a band of pinning solutions appears around the zero-frequency curve from the symmetric case, and that the band is delimited by curves of infinite-period bifurcations. The details of what happens when the infinite-period bifurcation curves approach the Hopf bifurcation curve are different in the five cases, and involve complicated dynamics with several codimension-two bifurcations occurring in a small region of parameter space as well as several global bifurcations.

Interest in the present analysis is twofold. First of all, although the details of the bifurcational process close to the zero-frequency Hopf point are very complicated and differ from case to case, for all cases, we observe the appearance of a pinning band delimited by infinite-period

bifurcations of homoclinic type that, away from the small region of complicated dynamics, are SNIC bifurcations, i.e. saddle–node on an invariant circle bifurcation [21]. Second, some of the scenarios analysed are important *per se*, as they correspond to the generic analysis of a partial breaking of the SO(2) symmetry, so that, after the introduction of perturbations, the system still retains a discrete symmetry (the Z_2 case is analysed in detail).

The paper is organized as follows. In §2, the properties of a Hopf bifurcation with SO(2) symmetry with the precession frequency crossing through zero are summarized, and the general unfolding of the SO(2) symmetry-breaking process is discussed. Section 3 explores the particulars of breaking the symmetry at orders zero, one and two. Section 3*b*,*c* is particularly interesting because it considers the symmetry-breaking processes $SO(2) \to Z_2$ and $SO(2) \to Z_3$, which are readily realized experimentally. Section 4 extracts the general features of the pinning problem from the analysis of the specific cases carried out in the earlier sections. Section 5 presents comparisons with experiments and numerical computations in two real problems in fluid dynamics, illustrating the application of the general theory developed in this study. Finally, conclusions and perspectives are presented in §6.

2. Hopf bifurcation with SO(2) symmetry and zero frequency

The normal form for a Hopf bifurcation is

$$\dot{z} = z(\mu + \mathrm{i}\omega - c|z|^2), \tag{2.1}$$

where z is the complex amplitude of the bifurcating periodic solution, μ is the bifurcation parameter, ω and c are functions of μ and generically at the bifurcation point ($\mu = 0$) both are different from zero. It is the non-zero character of ω that allows one to eliminate the quadratic terms in z in the normal form. This is because the normal form $\dot{z} = P(z, \bar{z})$ satisfies [22]

$$P(\mathrm{e}^{-\mathrm{i}\omega t} z, \mathrm{e}^{\mathrm{i}\omega t}\bar{z}) = \mathrm{e}^{-\mathrm{i}\omega t} P(z, \bar{z}), \tag{2.2}$$

where P is a low-order polynomial capturing the dynamics in a neighbourhood of the bifurcation point. If $\omega = 0$, this equation becomes an identity and P cannot be simplified. The case $\omega = 0$ is a complicated bifurcation that depends on the details of the double-zero eigenvalue of the linear part L of P. Because $z = x + \mathrm{i}y$ is complex, L is a real 2×2 matrix using the real coordinates (x, y). If L is not completely degenerate, that is

$$L = \begin{pmatrix} 0 & 1 \\ 0 & 0 \end{pmatrix}, \tag{2.3}$$

then we have the well-studied Takens–Bogdanov (TB) bifurcation, whereas the completely degenerate case,

$$L = \begin{pmatrix} 0 & 0 \\ 0 & 0 \end{pmatrix}, \tag{2.4}$$

is a high-codimension bifurcation that has not been completely analysed.

If the system has SO(2) symmetry, then it must also satisfy

$$P(\mathrm{e}^{\mathrm{i}m\theta} z, \mathrm{e}^{-\mathrm{i}m\theta}\bar{z}) = \mathrm{e}^{\mathrm{i}m\theta} P(z, \bar{z}), \tag{2.5}$$

where Z_m is the discrete symmetry retained by the bifurcated solution. When the group Z_m is generated by rotations of angle $2\pi/m$ about an axis of m-fold symmetry, as is usually the case with SO(2), then the group is also called C_m. Equations (2.2) and (2.5) are completely equivalent and have the same implications for the normal form structure. Advancing in time is the same

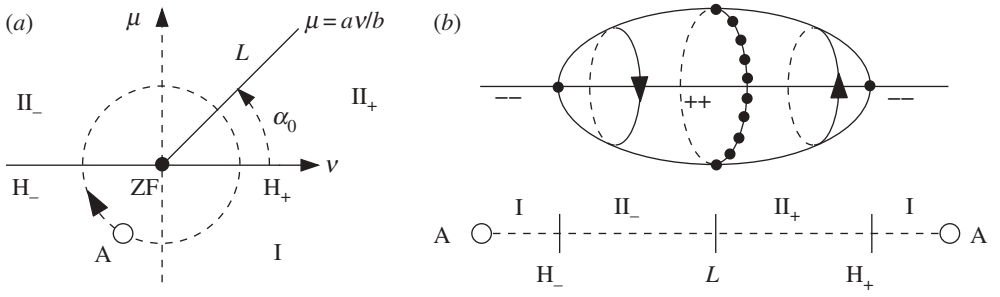

Figure 1. Hopf bifurcation with SO(2) symmetry and zero frequency; (*a*) the bifurcation diagram, where the thick lines are bifurcation curves, and (*b*) the bifurcations along the path A shown in (*a*). The fixed point curve is labelled with the signs of its eigenvalues. In regions II_- and II_+ the limit cycles, born at the Hopf bifurcations H_- and H_+, rotate in opposite senses. *L* is the line where the limit cycle becomes an invariant curve of fixed points.

as rotating the solution by a certain angle ($\omega t = m\theta$); the bifurcated solution is a rotating wave. Therefore, if ω becomes zero by varying a second parameter, then we still have the same normal form (2.1), owing to (2.5), with ω replaced by a small parameter ν,

$$\dot{z} = z(\mu + \mathrm{i}\nu - c|z|^2). \tag{2.6}$$

The Hopf bifurcation with SO(2) symmetry and zero frequency is, in this sense, trivial. Introducing the modulus and phase, $z = r\,\mathrm{e}^{\mathrm{i}\phi}$, the normal form becomes

$$\dot{r} = r(\mu - ar^2), \quad \dot{\phi} = \nu - br^2, \tag{2.7}$$

where $c = a + \mathrm{i}b$, and let us assume for the moment that a and b are positive. The bifurcation frequency in (2.7) is now the small parameter ν. The bifurcated solution RW_m exists only for $\mu > 0$, and has amplitude $r = \sqrt{\mu/a}$ and frequency $\omega = \nu - b\mu/a$. The limit cycle RW_m becomes an invariant set of steady solutions along the straight line $\mu = a\nu/b$ (labelled *L* in figure 1) where the frequency of RW_m goes to zero; the angle between *L* and the Hopf bifurcation curve (the horizontal axis $\mu = 0$) is α_0. The bifurcation diagram and schematic of the bifurcations along a one-dimensional path is also shown in figure 1. The zero-frequency Hopf bifurcation point (ZF), at $\mu = \nu = 0$, is of codimension-two. It coincides with the generic Hopf bifurcation, except that its phase portrait includes a line *L*, starting from the point ZF, along which the bifurcated solution has zero frequency.

Assuming $c \neq 0$, we can simplify (2.7) by scaling z so that $|c| = 1$; we will write

$$c = a + \mathrm{i}b = \mathrm{i}\,\mathrm{e}^{-\mathrm{i}\alpha_0} = \sin\,\alpha_0 + \mathrm{i}\cos\,\alpha_0, \quad b + \mathrm{i}a = \mathrm{e}^{\mathrm{i}\alpha_0}, \tag{2.8}$$

which helps simplify subsequent expressions. The cases a and b are both positive, which we will analyse in detail in the following sections, correspond to one of the fluid dynamics problems that motivated the present analysis (see [16,23] and §5*a*). For other signs of a and b, analogous conclusions can be drawn. It is of particular interest to consider the subcritical case $a < 0$ as it corresponds to the other fluid dynamics problem analysed here (see [24,25] and §5*b*). By reversing time and changing the sign of μ and ν, we obtain exactly the same normal form (2.7) but with the opposite sign of a and b. By changing the sign of ϕ and ν, we obtain (2.7) with the opposite sign of b. Therefore, all possible cases corresponding to different signs of a and b can be reduced to the case where a and b are both positive.

(a) Unfolding the Hopf bifurcation with zero frequency

If the SO(2) symmetry in the normal form (2.6) is completely broken, and no symmetry remains, then the restrictions imposed on the normal form by (2.5) disappear completely, and all the terms

in z and $\bar{z}$ missing from (2.6) will reappear multiplied by small parameters. This means that the normal form will be

$$\dot{z} = z(\mu + \mathrm{i}\nu - c|z|^2) + \epsilon_1 + \epsilon_2\bar{z} + \epsilon_3\bar{z}^2 + \epsilon_4 z\bar{z} + \epsilon_5 z^2, \tag{2.9}$$

where additional cubic terms have been neglected because we assume $c \neq 0$ and that $cz|z|^2$ will be dominant. As the ϵ_i are complex, we have a problem with 12 parameters. Additional simplifications can be made in order to obtain the so-called hypernormal form; this method is extensively used by Kuznetsov [26], for example. Unfortunately, many of the simplifications rely on having some low-order term in the normal form being non-zero with a coefficient of order one. For example, if $\omega \neq 0$, then it is possible to make c real by using a time re-parametrization. In our problem, all terms up to and including second order are zero or have a small coefficient, and so only a few simplifications are possible. These simplifications are an infinitesimal translation of z (two parameters), and an arbitrary shift in the phase of z (one parameter). Using these transformations, the 12 parameters can be reduced to nine. In particular, one of either ϵ_4 or ϵ_5 can be taken as zero and the other can be made real. By rescaling z, we can make c of modulus one, as in (2.8). A complete analysis of a normal form depending on nine parameters, i.e. a bifurcation of codimension of about nine, is completely beyond the scope of this paper. In the literature, only codimension-one bifurcations have been completely analysed. Most of the codimension-two bifurcations for ordinary differential equations and maps have also been analysed, except for a few bifurcations for maps that remain outstanding [26]. A few codimension-three and very few codimension-four bifurcations have also been analysed [27,28], but, to our knowledge, there is no systematic analysis of bifurcations of codimension greater than two.

In the following sections, we consider the five cases, ϵ_1 to ϵ_5, separately. A combination of analytical and numerical tools allows for a detailed analysis of these bifurcations. We extract the common features of the different cases when $\epsilon_i \ll \sqrt{\mu^2 + \nu^2}$, which captures the relevant behaviour associated with weakly breaking SO(2) symmetry. In particular, the ϵ_2 case exhibits very interesting and rich dynamics that may be present in some practical cases when the SO(2) symmetry group is not completely broken and a Z_2 symmetry group, generated by the half-turn $\theta \to \theta + \pi$, remains.

Some general comments can be made here about these five cases, which are of the form

$$\dot{z} = z(\mu + \mathrm{i}\nu - c|z|^2) + \epsilon z^q \bar{z}^{p-q}, \tag{2.10}$$

for integers $0 \leq q \leq p \leq 2$, excluding the case $p = q = 1$ which is SO(2) equivariant, and so ϵ can be absorbed into μ and ν. By changing the origin of the phase of z, we can modify the phase of ϵ so that it becomes real and positive. Then, by re-scaling z, time t, and the parameters μ and ν as

$$(z, t, \mu, \nu) \to (\epsilon^{\delta} z, \epsilon^{-2\delta} t, \epsilon^{2\delta}\mu, \epsilon^{2\delta}\nu), \quad \delta = \frac{1}{3-p}, \tag{2.11}$$

we obtain (2.10) with $\epsilon = 1$, effectively leading to codimension-two bifurcations in each of the five cases. We expect complex behaviour for $\mu^2 + \nu^2 \lesssim \epsilon^2$, when the three parameters are of comparable size, whereas the effects of small imperfections breaking SO(2) will correspond to $\mu^2 + \nu^2 \gg \epsilon^2$. From now on $\epsilon = 1$ will be assumed, and we can restore the explicit ϵ-dependence by reversing the transformation (2.11). Three of the five normal forms (2.11) have been analysed in the literature (discussed below), focusing on the regions where μ, ν and ϵ are of comparable size; here we will also consider what happens for $\mu^2 + \nu^2 \gg \epsilon^2$, which is particularly important for the pinning phenomenon.

3. Bifurcation diagrams for the five symmetry-breaking cases

The normal forms corresponding to the ϵ_1, ϵ_2 and ϵ_3 cases have already been analysed in contexts completely different from the SO(2) symmetry-breaking context considered here. The context in which these problems were studied stems from low-order resonances in perturbed Hopf problems. Time-periodic forcing near a Hopf bifurcation point has previously been studied [17],

analysing the problem using the Poincaré stroboscopic map. The normal forms corresponding to the 1 : 1, 1 : 2 and 1 : 3 strong resonances coincide with the normal forms we present below for cases with only the ϵ_1, ϵ_2 and ϵ_3 terms retained in (2.9), respectively. Later, motivated by a problem of a nonlinear oscillator with damping and quasi-periodic driving, a series of papers extended the strong resonance results of Gambaudo [17] by studying the semi-global bifurcations for periodically and quasi-periodically perturbed driven damped oscillators near a Hopf bifurcation (see [18–20] and references therein). The other two cases we consider, with only the ϵ_4 or the ϵ_5 terms retained in (2.9), do not appear to have been studied previously. They fall outside the context in which the other three were studied because they do not correspond to any canonical resonance problem. We should point out that, within the resonance context, the three cases studied would not make sense to consider in combination (they correspond to completely distinct frequency ratios and so would not generically occur in a single problem). By contrast, within the context motivating our study, all five cases correspond to different ways in which the SO(2) symmetry of a system may be broken, and, in a physical realization, all five could coexist. In the following sections, we present a short summary of the results. A detailed analysis of all five cases can be found in Marques *et al.* [29].

(a) Symmetry breaking of SO(2) with an ϵ term

The normal form in this case is (2.10) with $p = q = 0$ and $\epsilon = 1$:

$$\dot{z} = z(\mu + \mathrm{i}\nu - c|z|^2) + 1. \tag{3.1}$$

This case has been analysed previously [17–20].

The fixed points of (3.1) are given by a cubic equation. The parameter space is divided into two regions: region III has three fixed points, and the rest of the parameter space has one fixed point, separated by a saddle–node curve shown in figure 2*a* as a thick black line. The saddle–node curve is divided into three different arcs $\mathrm{SN}_\pm$ and SN_0 by two codimension-two cusp bifurcation points, $\mathrm{Cusp}_\pm$. The fixed points also undergo Hopf bifurcations along the curves $\mathrm{H}_\pm$ shown in grey in figure 2*a*. Figure 2*b* shows what happens when the ϵ dependence is restored; what we have is that figure 2*a* just scales with ϵ as indicated in (2.11), and the pinning region collapses onto the line L of the perfect case with SO(2) symmetry. For $|\nu| \to \infty$, the Hopf curves $\mathrm{H}_\pm$ are asymptotic to the $\mu = 0$ axis, the Hopf curve for $\epsilon = 0$. The other ends of the $\mathrm{H}_\pm$ curves are the TB points $\mathrm{TB}_\pm$ on the saddle–node curve. The TB_- and Cusp_- codimension-two bifurcation points are very close to each other. For clarity in the schematic shown in figures 2*a* and 3, we have exaggerated their separation. In region I, there is a single stable fixed point. It loses stability along the Hopf curves $\mathrm{H}_\pm$; so in regions $\mathrm{II}_\pm$, there exist an unstable fixed point and a stable rotating wave; the rotating waves in $\mathrm{II}_\pm$ rotate in opposite directions and III is the pinning region where the rotation stops and we have a stable fixed point. Solutions with $\omega = 0$, which existed only along a single line in the absence of imperfections, now exist in a region of finite width.

From the TB points, dynamical systems theory says that two curves of homoclinic bifurcations emerge, resulting in global bifurcations around these points. Moreover, the stable limit cycles in regions $\mathrm{II}_\pm$ do not exist in region III, so they must disappear in additional bifurcations. Figure 3 summarizes all the bifurcation curves that appear in the present case. There are nine codimension-two points organizing the dynamics of the normal form (3.1), and most of the bifurcation curves correspond to global bifurcations of limit cycles; they are described in detail in Marques *et al.* [29]. For large values of $\mu^2 + \nu^2$, the stable limit cycles in regions $\mathrm{II}_\pm$ disappear at $\mathrm{SNIC}_\pm$ (saddle–node on an invariant circle) bifurcation curves. On these curves, a saddle–node bifurcation of fixed points takes place on top of the limit cycle, and the cycle disappears in an infinite-period bifurcation. What remains, and is observable, is the stable fixed point born at the saddle–node.

The width w of the pinning region at a distance $d = \sqrt{\mu^2 + \nu^2}$ from the origin is measured transversally to the straight line L. In the case considered here, it is given by $w = 2/\sqrt{d}$. Restoring the ϵ-dependence, we obtain $w(d, \epsilon) = 2\epsilon/\sqrt{d}$. The pinning region becomes narrower

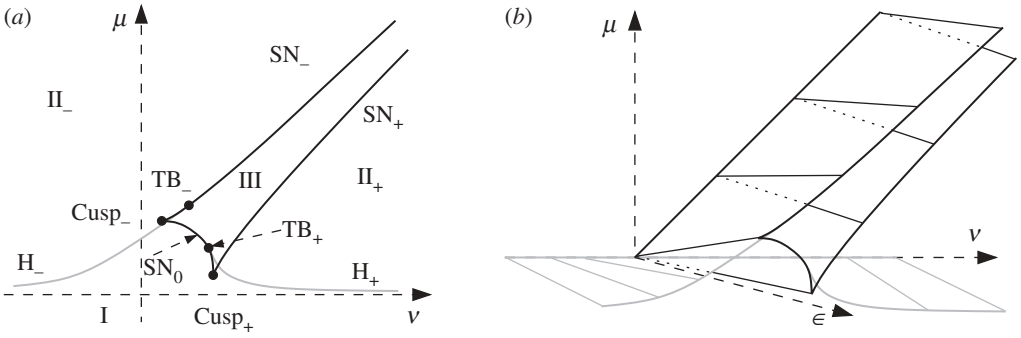

Figure 2. (*a*) Bifurcations of the fixed points corresponding to the normal form (3.1), and (*b*) is a perspective view of the corresponding codimension-three bifurcation in terms of (μ, ν, ϵ). See table 1 for a glossary.

Table 1. Glossary of bifurcations.

	codimension-one bifurcations
$SN_{\pm,0}$	saddle–node (also called fold) bifurcations
$H_{\pm,0}$	Hopf bifurcations
$PF_{\pm}$	pitchfork bifurcations
CF	cyclic fold: two limit cycles are born simultaneously
$L, L_{l,u}$	limit cycle becoming a family of fixed points
$Hom_{\pm,0}$, Hom	homoclinic collision of a limit cycle with a saddle
$Het_{\pm,0}$	heteroclinic collision of a limit cycle with saddles
$SNIC_{\pm,0}$	saddle–node appearing on a limit cycle
Glu	gluing bifurcation-two limit cycles collide with a saddle
	codimension-two bifurcations
$cusp_{\pm}$	cusp bifurcations
$TB_{\pm}$, TB	Takens-Bogdanov bifurcations
$dPF_{\pm}$	degenerate pitchfork-zero cubic term
Ba	Bautin bifurcation–degenerate Hopf with zero cubic term
PfGl	simultaneous gluing Gl and pitchfork PF bifurcations
CfHom	simultaneous cyclic-fold CF and homoclinic collision Hom
$CfHet_{\pm}$	simultaneous cyclic-fold CF and heteroclinic collision Hom
$SnicHom_{\pm,0}$	simultaneous SNIC and homoclinic collision
$SnicHet_{\pm,0}$	simultaneous SNIC and heteroclinic collision

with increasing distance from the bifurcation point, and its width is proportional to ϵ, the magnitude of the imperfection (figure 2*b*).

(b) Symmetry breaking of SO(2) to Z_2: the $\epsilon\bar{z}$ case

The $\epsilon_2\bar{z}$ term in (2.9) corresponds to breaking SO(2) symmetry in a way that leaves a system with Z_2 symmetry. The normal form is (2.10) with $p = 1$, $q = 0$ and $\epsilon = 1$,

$$\dot{z} = z(\mu + \mathrm{i}\nu - c|z|^2) + \bar{z}. \tag{3.2}$$

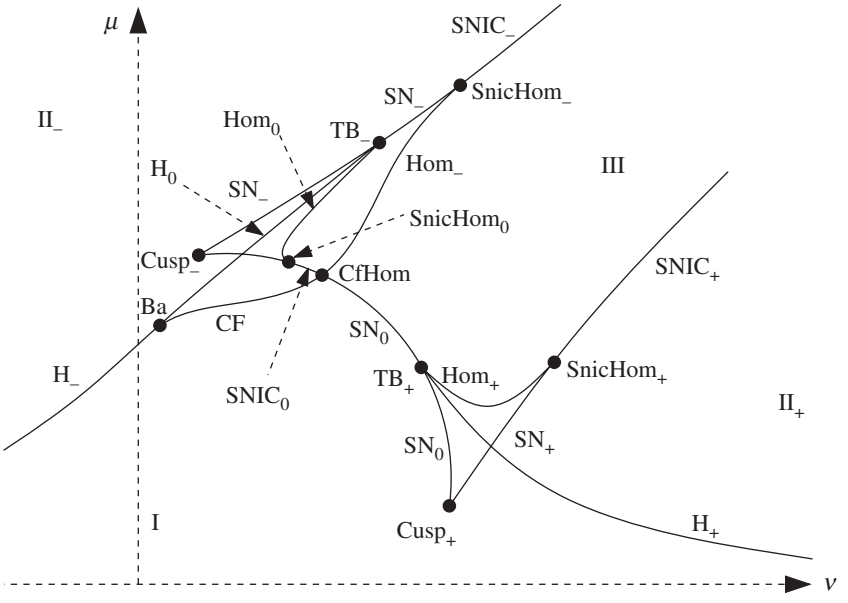

Figure 3. Schematic of the bifurcations of the normal form (3.1). See table 1 for a glossary.

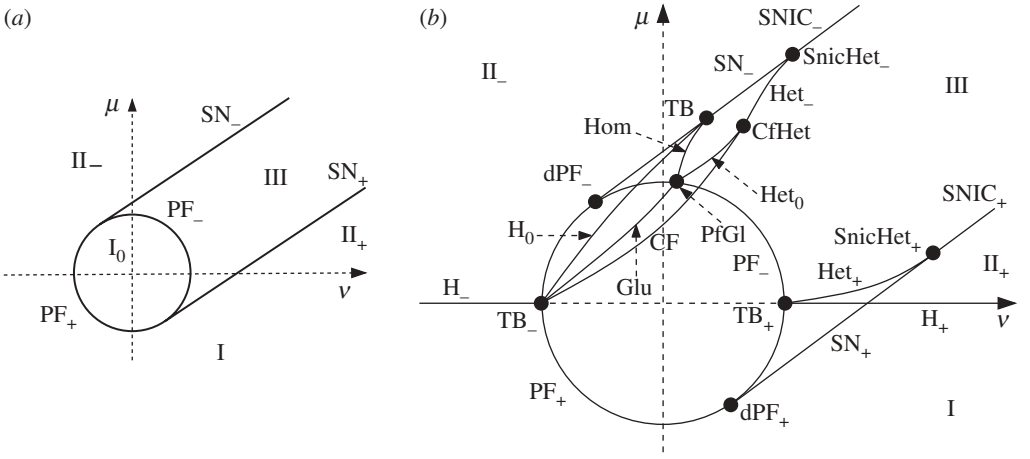

Figure 4. (*a*) Bifurcations of the fixed points corresponding to the normal form (3.2). (*b*) Global bifurcations in the symmetry breaking of the SO(2) to Z_2 case. See table 1 for a glossary.

The normal form (3.2) is invariant to $z \to -z$, or, equivalently, the half-turn $\theta \to \theta + \pi$. This is all that remains of the SO(2) symmetry group. In fact, this Z_2 symmetry implies that $P(z, \bar{z})$ in $\dot{z} = P(z, \bar{z})$ must satisfy (2.5) for $\theta = \pi$. In other words, P must be odd: $P(-z, -\bar{z}) = -P(z, \bar{z})$. Therefore, (3.2) is the unfolding corresponding to the symmetry breaking of SO(2) to Z_2. This case has also been analysed previously [17–20].

The normal form (3.2) admits up to five fixed points. One is the trivial solution $r = 0$; the other fixed points come in two pairs of Z_2-symmetric points. There are three different regions in the (μ, ν)-parameter plane shown in figure 4*a*: region III with five fixed points, bounded by two parallel straight lines and the half unit circle PF_-; region I_0 with three fixed points, bounded by the circle of radius one; and the remaining parameter space with one fixed point. These three regions are separated by four curves along which steady bifurcations between the different fixed points take place, as shown in figure 4*a*. $\mathrm{PF}_\pm$ are curves of pitchfork bifurcations, and $\mathrm{SN}_\pm$ are

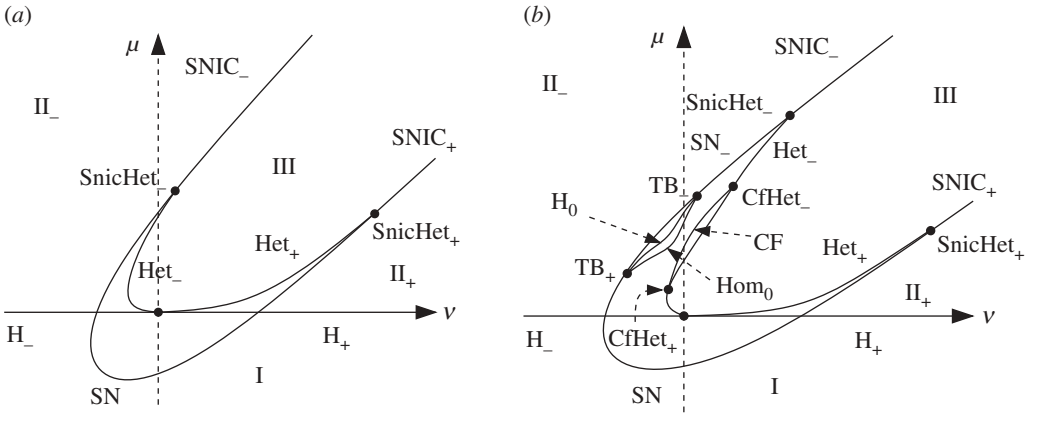

Figure 5. Schematic of bifurcation curves corresponding to the normal form with quadratic terms (3.3) in the $\epsilon\bar{z}^2$ case for (*a*) $\alpha_0 > \pi/6$ and (*b*) $\alpha_0 < \pi/6$. H_0 is tangent to the parabola at the Takens–Bogdanov points $TB_\pm$; H_0 and Hom_0 almost coincide with SN_-.

saddle–node bifurcation curves. Figure 4*b* also includes the Hopf curves $H_\pm$ that coincide with the Hopf curves in the unperturbed case for $|\nu| > 1$, and terminate at the two TB points $TB_\pm$. Solutions with zero frequency, which existed only along a single line L in the absence of imperfections, now exist in the region bounded by the semi-circle and the two half-lines; this region III is the pinning region.

Again, we can ask about the fate of the stable limit cycles approaching the pinning region, and about the global bifurcations emerging from the TB points. The resulting scenario is very complex. A schematic of all local and global bifurcation curves is shown in figure 4*b*. There are nine codimension-two points, and a variety of curves where global bifurcations of limit cycles take place. The details are in the mentioned references, and in particular in Marques *et al.* [29]. As in the previous case, §3*a*, with increasing $\mu^2 + \nu^2$, the saddle–node appears precisely on the limit cycle, resulting in a SNIC bifurcation. The width of the pinning region is constant: $w = 2$. On restoring the ϵ-dependence, we obtain a width $w(d, \epsilon) = 2\epsilon$ independent of the distance to the bifurcation point and proportional to the magnitude of the imperfection.

(c) Symmetry breaking of SO(2) to Z_3: the $\epsilon\bar{z}^2$ case

The $\epsilon_3\bar{z}^2$ term in (2.9) corresponds to breaking SO(2) symmetry in a way that leaves a system with Z_3 symmetry. The normal form to be analysed in this case is

$$\dot{z} = z(\mu + \mathrm{i}\nu - c|z|^2) + \bar{z}^2. \tag{3.3}$$

This normal form is invariant to rotations $\theta \to \theta \pm 2\pi/3$, or equivalently to $z \to \exp(\pm 2\pi \mathrm{i}/3)z$. $P(z, \bar{z})$ must satisfy (2.5) for $\theta = \pm 2\pi/3$, and the only ϵ_j term in (2.9) satisfying this condition is $\epsilon_3\bar{z}^2$. Therefore, (3.3) is the unfolding corresponding to the symmetry breaking of SO(2) to Z_3. This case has been analysed previously [17,19].

The normal form (3.3) admits up to seven fixed points, the trivial solution $r = 0$ and two triplets of Z_3-symmetric points. There are different regions in the (μ, ν)-parameter plane. Region III, with seven fixed points, is the interior of the parabola in figure 5, and is the pinning region. The parabola is a curve of saddle–node bifurcations, where the two triplets of steady points are simultaneously born, one triplet being stable and the other unstable. Region I is below the horizontal axis and outside the parabola, where there is only one fixed point $r = 0$. This $r = 0$ fixed point, which exists in all parameter space, is stable below the $\mu = 0$ axis, and it loses stability along the Hopf bifurcation curves $H_\pm$ at the horizontal $\mu = 0$ axis, delimiting regions $II_\pm$. These regions are outside the parabola and above the $\mu = 0$ axis, where there is one unstable fixed point and a stable rotating wave, which rotates in opposite senses in $II_\pm$.

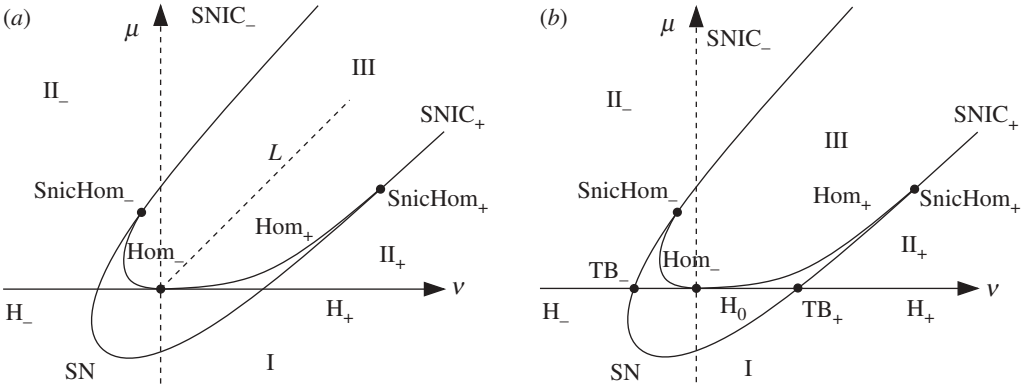

Figure 6. Schematic of bifurcation curves corresponding to the normal forms with (*a*) quadratic terms in the $\epsilon z\bar{z}$ case (3.4) and (*b*) quadratic terms in the ϵz^2 case (3.5).

In this case, there are also additional codimension-two points and curves of global bifurcations. There are two different scenarios depending on the value of the angle α_0. Figure 5*a* corresponds to $\alpha_0 > \pi/6$ with three codimension-two points, and figure 5*b* corresponds to $\alpha_0 < \pi/6$ with seven codimension-two points. As in the previous cases, for large values of $d = \sqrt{\mu^2 + \nu^2}$, the limit cycles in regions $\mathrm{II}_\pm$ undergo $\mathrm{SNIC}_\pm$ bifurcations on the parabola and disappear at the border of the pinning region. The scaling of the width of the pinning region with ϵ is discussed at the end of the next section, because all the quadratic cases share the same scaling.

(d) The quadratic $\epsilon_4 z\bar{z}$ and $\epsilon_5 z^2$ cases

These two cases are new and have not been considered in the literature to the best of our knowledge, because they do not appear in the context of low-order resonances in perturbed Hopf problems. These two cases have a much simpler dynamics than the previously considered three cases, and are very similar to the simple scenario in the quadratic $\epsilon_3\bar{z}^2$ depicted in figure 5*a*. The corresponding normal forms are

$$\dot{z} = z(\mu + \mathrm{i}\nu - c|z|^2) + z\bar{z} \tag{3.4}$$

and

$$\dot{z} = z(\mu + \mathrm{i}\nu - c|z|^2) + z^2. \tag{3.5}$$

The two cases have three fixed points in the interior of the same parabola as in the $\bar{z}^2$ case. The parabola is a saddle–node bifurcation curve, and, outside of it, there exists only one fixed point, the trivial solution $z = 0$, that also undergoes a Hopf bifurcation along the curve $\mu = 0$. The difference with the previous quadratic case is that the Z_3 symmetry does not exist, and in fact the SO(2) symmetry is completely broken. Therefore, the two triplets of solutions that existed in the $\bar{z}^2$ case reduce to a pair of fixed points in the present cases. Another difference is in the dynamics associated with the codimension-two points and global bifurcations of limit cycles. Figure 6*a*,*b* shows schematics of all the local and global bifurcations in the two cases. Figure 6*a* corresponds to (3.4) and is identical to figure 5*a* with three codimension-two points, except that at the saddle–node curves only one pair of fixed points is born. Figure 6*b* corresponds to (3.5) and is more complicated. There are five codimension-two points, including two additional TB points, $\mathrm{TB}_\pm$, connected by a homoclinic curve, H_0. Along this curve, the phase portrait has a homoclinic connection whose interior is filled with a continuous family of periodic orbits. This peculiar degenerate feature is analysed in detail in Marques *et al.* [29], and it will not appear in real systems because the normal form (3.5) is not the unfolding of some symmetric case; it will always appear in combination with the other cases discussed previously.

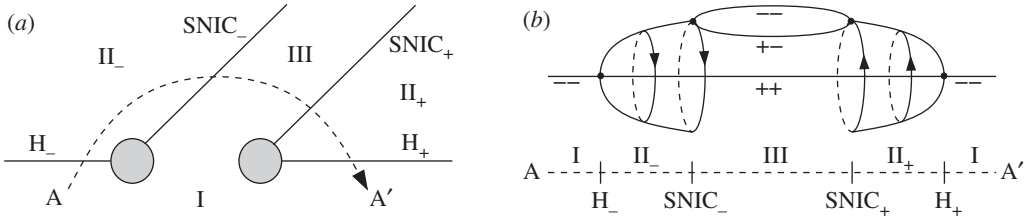

Figure 7. An imperfect Hopf bifurcation under general perturbations; (*a*) the various regions in parameter space and (*b*) a bifurcation diagram along the one-dimensional path A–A′. The signs $(++, --, +-)$ indicate the sign of the real part of the two eigenvalues of the solution branch considered.

A common feature of the two cases considered here is the presence of $\mathrm{SNIC}_{\pm}$ bifurcation curves away from the origin in (μ, ν)-parameter space, as in the previously analysed cases. In the three quadratic cases, the pinning region is delimited by the same parabola, and the width of the pinning region is given by $w = 2\sqrt{d}$, resulting in $w(d, \epsilon) = 2\epsilon\sqrt{d}$ when the dependence on ϵ is restored. The width of the pinning region increases with the distance d to the bifurcation point, and is proportional to the magnitude of the imperfection ϵ.

4. Common features in the different ways to break SO(2) symmetry

Here we summarize the features that are common to the five different perturbations analysed in the previous sections. The most important feature is that the curve of zero frequency splits into two curves with a region of zero-frequency solutions appearing in between (the so-called pinning region). Of the infinite number of steady solutions that exist along the zero-frequency curve in the *perfect* system with SO(2) symmetry (figure 1*b*), only a small finite number remain. These steady solutions correspond to the pinned solutions observed in experiments and in numerical simulations, such those to be described in §5. The number of remaining steady solutions depends on the details of the symmetry-breaking imperfections, but when SO(2) is completely broken and no discrete symmetries remain, there are three steady solutions in the pinning region III (figure 7*a*). One corresponds to the base state, now unstable with eigenvalues $(+, +)$. The other two are born on the $\mathrm{SNIC}_{\pm}$ curves delimiting region III away from the origin. Of these two solutions, one is stable (the only observable state in region III) and the other is a saddle (figure 7*b*). There are also the two Hopf bifurcation curves H_- and H_+. The regions where the Hopf bifurcations meet the infinite-period bifurcations cannot be described in general, and, as has been shown in the examples in the previous sections, will depend on the specifics of how the SO(2) symmetry is broken, i.e. on the specifics of the imperfections present in the problem considered. These regions contain complex bifurcational processes, and are represented as grey discs in figure 7*a*. The stable limit cycle existing outside III, in regions $\mathrm{II}_{\pm}$, undergoes a SNIC bifurcation and disappears upon entering region III (figure 7*b*). When the $\mathrm{SNIC}_{\pm}$ bifurcation curves approach the Hopf bifurcation curves (i.e. enter the grey disc regions), the saddle–node bifurcations do not occur on the stable limit cycle but very close by, and the limit cycle disappears in a saddle–loop homoclinic collision that occurs very close to the saddle–node bifurcations.

In all cases considered, the curves delimiting the pinning region away from the origin are SNIC bifurcations, and dynamical systems theory provides a simple argument for this. Consider the generalization of (2.10); writing $z = r\,\mathrm{e}^{\mathrm{i}\theta}$ in polar coordinates gives

$$\dot{r} = r(\mu - ar^2) + \epsilon F_1(r, \theta), \quad \dot{\theta} = \nu - br^2 + \epsilon F_2(r, \theta), \tag{4.1}$$

where F_i is periodic in θ. Away from the origin, μ and ν are non-zero, and $\epsilon \ll \mu, \nu$. For sufficiently small ϵ, there exists an attracting invariant circle [26]. Therefore, letting $r^2 \to \mu/a$ (plus order ϵ terms) in the phase equation results in

$$\dot{\theta} = \nu - \frac{b\mu}{a} + \epsilon f(\theta) = \zeta + \epsilon f(\theta), \tag{4.2}$$

where f is periodic in θ. We have introduced the detuning parameter $\zeta = \nu - b\mu/a$, proportional to the distance from the point (μ, ν) to the straight line L (the zero-frequency line in the perfect system; figure 1*a*). If the detuning parameter is large, the invariant circle is a periodic solution with frequency $\approx \zeta$. If $\zeta = O(\epsilon)$, the dynamics is more complicated. In the five cases considered here, $f(\theta) = k \sin m\theta$, and (4.2) is the well-known Adler equation [30], the continuous version of the Arnold circle map. Both equations have regions in parameter space where phase-locking takes place (Arnold's tongues). For the Adler equation, fixed points exist inside the region $\zeta \in [-k\epsilon, k\epsilon]$ that originate on the boundary of the region in saddle–node bifurcations taking place on the invariant circle, i.e. SNIC bifurcations. Moreover, the width of the pinning region away from the origin is proportional to ϵ.

In all cases considered, the width of the pinning region scales linearly with the magnitude of the symmetry-breaking imperfection ϵ. We have found $w(d, \epsilon) = 2\epsilon d^{(p-1)/2}$, where $p = 0, 1, 2$ is the order of the symmetry breaking considered (2.10). For lower order terms, the width decreases (in the zero-order ϵ case) or remains constant (in the first-order $\epsilon\bar{z}$ case) with increasing distance from the bifurcation point. For quadratic terms, the width increases with the distance. When arbitrary perturbations are included, we expect a behaviour of the form $w(d, \epsilon) = \epsilon f(d)$, where the function f will depend on the details of the symmetry-breaking terms involved. The size of the regions containing complex bifurcational processes (the grey discs in figure 7*a*) is of order ϵ or smaller, as we have seen in all cases considered. Therefore, these regions are comparable in size or smaller than the width of the pinning region.

Of the five scenarios analysed, two of the cases correspond to breaking the SO(2) symmetry to Z_m, for $m = 2$ and $m = 3$ or Z_3. For $m \geq 4$, the symmetry-breaking dynamics is much simpler because the additional terms in the normal form are of order higher than three. They have been analysed previously [17,29], and are very similar to the weakly resonant Neimark–Sacker bifurcation [26]. The width of the pinning region at a distance d from the origin is given by $w(d) = 2\epsilon d^{(m-2)/2}$. The boundaries of the pinning region are SNIC bifurcation curves, and the width of the pinning region is proportional to the magnitude of the imperfection ϵ, as in the five cases analysed in the preceding section.

Another common feature is that the $\mathrm{SNIC}_{\pm}$ bifurcations, where the stable limit cycle disappears on entering the pinning region away from the origin ($\mu = \nu = 0$), become homoclinic or heteroclinic collisions close to the origin. There is a codimension-two global bifurcation, SnicHom, where the SNIC, saddle–node and homoclinic collision curves meet. This bifurcation is discussed in detail in Marques *et al.* [29]. It has important implications, because the scaling laws for the period of the limit cycle approaching either a SNIC or a homoclinic collision are different: the scaling is square-root for a SNIC bifurcation and logarithmic for a homoclinic collision. When the interval between the SN_{-} bifurcation and the homoclinic collision is very small, it cannot be resolved experimentally, or even numerically in an extended system such as the Navier–Stokes equations. In such a situation, the square-root fit appears adequate, because, away from the SN_{-} point, the dynamical system just feels the ghost of the about-to-be-formed saddle–node pair and does not distinguish between whether the saddle–node appears on the limit cycle or just very close to it. However, if the very narrow parameter range between the saddle–node formation and the subsequent collision with the saddle can be resolved, then the log fit matches the period in this narrow interval much better.

5. Fluid dynamics examples of pinning owing to breaking the SO(2) symmetry

(a) Pinning in small aspect ratio Taylor–Couette flow

Experiments in small aspect ratio Taylor–Couette flows have reported the presence of a band in parameter space where rotating waves become steady non-axisymmetric solutions (a pinning effect) via infinite-period bifurcations [31]. Previous numerical simulations, assuming SO(2)

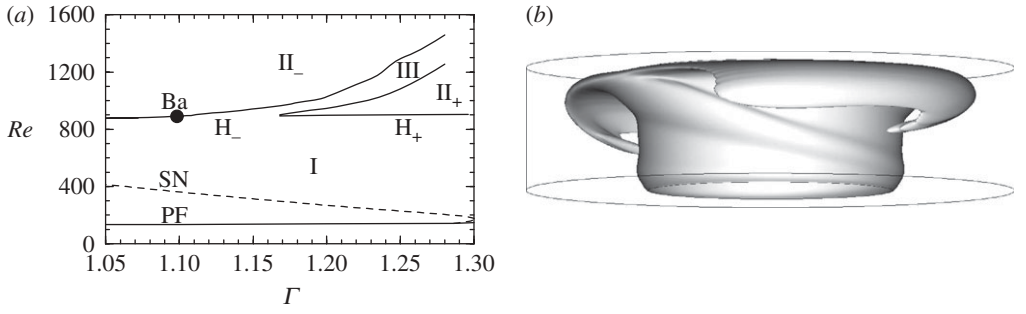

Figure 8. (*a*) Experimental regimes found in the small aspect ratio Taylor–Couette problem, with a pinning region, adapted from Pfister *et al*. [31]. (*b*) Numerically computed rotating wave at $Re = 1200$, $\Gamma = 1$ and $\eta = 0.5$, adapted from Marques & Lopez [32], typical of those found in regions $\mathrm{II}_{\pm}$.

symmetry of the apparatus, were unable to reproduce these observations [32]. Recent additional experiments suggest that the pinning effect is not intrinsic to the dynamics of the problem, but rather is an extrinsic response induced by the presence of imperfections that break the SO(2) symmetry of the ideal problem. Additional controlled symmetry-breaking perturbations were introduced into the experiment by tilting one of the endwalls [16]. Direct numerical simulations of the Navier–Stokes equations including the tilt of one endwall by a very small angle have been conducted [23]. Those simulations agree very well with the experiments, and the normal form theory developed in this paper provides a theoretical framework for understanding the observations.

Taylor–Couette flow consists of a fluid confined in an annular region of inner and outer radii r_i and r_o, capped by endwalls a distance h apart. The endwalls and the outer cylinder are stationary, and the flow is driven by the rotation of the inner cylinder at constant angular speed Ω. The system is governed by three parameters: the Reynolds number, $Re = \Omega r_i(r_o - r_i)/\nu$, the aspect ratio, $\Gamma = h/(r_o - r_i)$, and the radius ratio, $\eta = r_i/r_o$, where ν is the kinematic viscosity. The system is invariant to arbitrary rotations about the axis, SO(2) symmetry, and to reflections about the mid-height, a Z_2 symmetry that commutes with SO(2). In both the experiments and the numerical simulations, the radius ratio was kept fixed at $\eta = 0.5$, and Re and Γ were varied.

For small Re, below the curve PF in figure 8*a*, the flow is steady, axisymmetric and reflection symmetric, consisting of two meridional cells [32]. The Z_2 reflection symmetry is broken in a pitchfork bifurcation along the curve PF, and a pair of steady axisymmetric one-cell states that have a jet of angular momentum emerging from the inner cylinder boundary layer near one or other of the endwalls is born. Both are stable, and which is realized depends on initial conditions. The only symmetry of these symmetrically related solutions is SO(2). These steady axisymmetric one-cell states are stable in region I. There are other flow states that are stable in this same region. For example, above the dashed curve SN in figure 8*a*, the two-cell state becomes stable and coexists with the one-cell states. However, the two-cell and the one-cell states are well separated in phase space and the experiments and numerics we describe below are focused on the one-cell state. On increasing Re, the one-cell state suffers a Hopf bifurcation that breaks the SO(2) symmetry and a rotating wave state emerges with azimuthal wavenumber $m = 2$. Figure 8*b* shows an isosurface of axial angular momentum, illustrating the three-dimensional structure of the rotating wave. For slight variations in aspect ratio, the rotating wave may precess either prograde (in region II_+ above H_+) or retrograde (in region II_- above H_-) with the inner cylinder, and in between a pinning region III is observed. This is observed even with a nominally perfect experimental system, i.e. with the SO(2) symmetry to within the tolerances in constructing the apparatus. The Hopf bifurcation is supercritical around the region where the precession frequency changes sign. However, for smaller aspect ratios the Hopf bifurcation becomes subcritical at the Bautin point Ba in figure 8*a*.

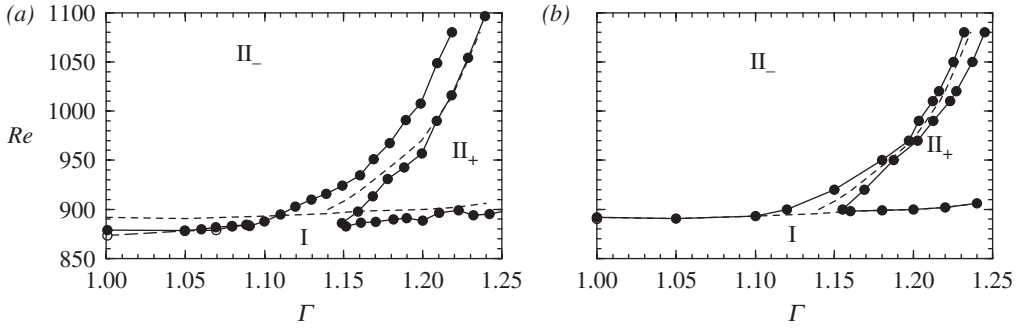

Figure 9. Bifurcation diagrams for the one-cell state from (*a*) the experimental results of Abshagen *et al.* [16] with natural imperfections, and (*b*) the numerical results of Pacheco *et al.* [23] with a tilt of 0.1° on the upper lid. The dotted curve in both is the numerically determined Hopf curve with zero tilt.

Various different experiments in this regime have been conducted in the nominally perfect system, as well as with a small tilt of an endwall [16,31,33,34]. Figure 9*a* shows a bifurcation diagram from the laboratory experiments of Abshagen *et al*. [16]. These experiments show that, without an imposed tilt, the natural imperfections of the system produce a measurable pinning region, and that the additional tilting of one endwall increases the extent of the pinning region. Tilt angles of the order of 0.1° are necessary for the tilt to dominate over the natural imperfections. Figure 9*b* shows a bifurcation diagram from the numerical results of Pacheco *et al*. [23], including a tilt of one of the endwalls of about 0.1°, showing very good agreement with the experimental results. Included in figure 9*a*,*b* is the numerically computed bifurcation diagram in the perfect system, shown as dotted curves. The effects of imperfections are seen to be important only in the parameter range where the Hopf frequency is close to zero and a pinning region appears. It is bounded by infinite-period bifurcations of limit cycles. The correspondence between these results and the normal form theory described in this paper is excellent, strongly suggesting that the general remarks on pinning extracted from the analysis of the five particular cases are indeed realized both experimentally and numerically. These two studies [16,23] are the only cases we know of where quantitative data about the pinning region are available. Yet, even in these cases, the dynamics close to the intersection of the Hopf curve with the pinning region, which according to our analysis should include complicated bifurcational processes, has not been explored either numerically or experimentally. This is a very interesting problem that deserves further exploration.

(b) Pinning in rotating Rayleigh–Bénard convection

Up to now, we have considered the zero-frequency Hopf problem in the context of a supercritical Hopf bifurcation. However, in the Taylor–Couette example discussed in the previous section, the zero frequency occurs quite close to a Bautin bifurcation, at which the Hopf bifurcation switches from being supercritical to subcritical, and a natural question is what are the consequences of the zero frequency occurring on a subcritical Hopf bifurcation. The normal form theory for the behaviour local to the Hopf bifurcation carries over by changing the direction of time and the sign of the parameters μ and ν as discussed before, but then both the limit cycle and the pinned state are unstable and not observable in a physical experiment or direct numerical simulation. The limit cycle becomes observable as it undergoes a saddle–node of limit cycle (a cyclic fold) bifurcation at the fold associated with the Bautin bifurcation (figure 10*a*), and we expect that the pinned state does likewise with a saddle–node of fixed points bifurcation along the same fold. In this section, we identify a rotating convection problem where precisely this occurs [24,25], and conduct new numerical simulations by introducing an SO(2) symmetry-breaking bifurcation that produces a pinning region on the upper branch of the subcritical Hopf bifurcation.

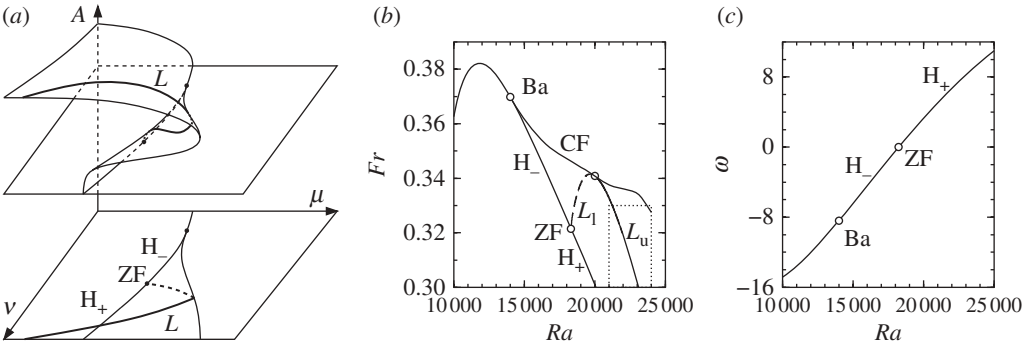

Figure 10. (*a*) Schematic of the Bautin bifurcation, including the path L of frequency zero bifurcated states in the SO(2) perfect system, shown in a two-parameter space (μ, ν) with A a global measure of the solution. Also shown is the projection of the saddle–node surface on parameter space. (*b*) Bifurcation curves for $\Omega = 100$, $\sigma = 7$ and $\gamma = 1$, where $H_{\mp}$ are the segments of the Hopf bifurcation with negative and positive frequency, the Bautin point Ba is where the Hopf bifurcation switches from super- to subcritical and the cyclic-fold bifurcation curve CF emerges. The lines L_l and L_u are the loci where the rotating wave has zero frequency on the lower and upper branches of the cyclic fold. The rectangle around L_u corresponds to figure 11*a*. (*c*) The frequency along the Hopf bifurcation $H_{\mp}$ with the Bautin point and the point ZF, where the sense of precession changes, marked as open symbols.

The rotating convection problem consists of a fluid-filled cylinder of radius r_0 and height h, rotating at a constant rate $\omega\,\mathrm{rad\,s^{-1}}$. The cold top and hot bottom endwalls are maintained at constant temperatures $T_0 \mp 0.5\Delta T$, where T_0 is the mean temperature and ΔT is the temperature difference between the endwalls. The sidewall has zero heat flux. The system is governed by five parameters: the Rayleigh number, $Ra = \alpha g h^3 \Delta T/(\kappa\nu)$, the Froude number, $Fr = \omega^2 r_0/g$, the Coriolis number, $\Omega = \omega h^2/\nu$, the Prandtl number, $\sigma = \nu/\kappa$, and the aspect ratio, $\gamma = r_0/h$, where α is the coefficient of volume expansion, g is the gravitational acceleration, κ is the thermal diffusivity and ν is the kinematic viscosity. For any $Fr \neq 0$, the system is not invariant to the so-called Boussinesq symmetry corresponding to invariance to a reflection K_z about the half-height $z = 0$. The system is invariant only under rotations about the axis of the cylinder, the SO(2) symmetry.

The governing equations have been solved using a second-order time-splitting method combined with a pseudo-spectral method for the spatial discretization, using a Galerkin–Fourier expansion in the azimuthal coordinate θ and Chebyshev collocation in r and z. The details are presented in Mercader *et al.* [35]. We have used $n_r = 36$, $n_\theta = 40$ and $n_z = 64$ spectral modes in r, θ and z and a time step $\mathrm{d}t = 2 \times 10^{-5}$ thermal time units in all computations. We have checked the spectral convergence of the code using the infinity norm of the spectral coefficients of the computed solutions. The trailing coefficients of the spectral expansions are at least five orders of magnitude smaller than the leading coefficients. In order to compute the zero-frequency line L in the subcritical region of the Bautin bifurcation, where the fixed points and limit cycles involved are unstable, we have used arclength continuation methods for fixed points and for rotating waves adapted to our spectral codes [36,37].

Figure 10*b* shows the parameter region of interest in this convection problem. In the region of high Froude number (region I), we have a stable steady solution, consisting of a single axisymmetric convective roll where the warm fluid moves upwards close to the axis (due to the rotation of the container), and returns along the sidewall. This base state loses stability when the Froude number Fr decreases, in a Hopf bifurcation along the curves $H_{\pm}$. The bifurcation is supercritical for $Ra < 14\,157$ and subcritical for higher Ra; the change from supercritical to subcritical happens at the codimension-two Bautin bifurcation point Ba, at $(Ra, Fr) \approx (14\,157, 0.3684)$. The bifurcated limit cycle, a rotating wave with azimuthal wave number $m = 3$, is unstable, but becomes stable at the cyclic fold curve CF (a saddle–node

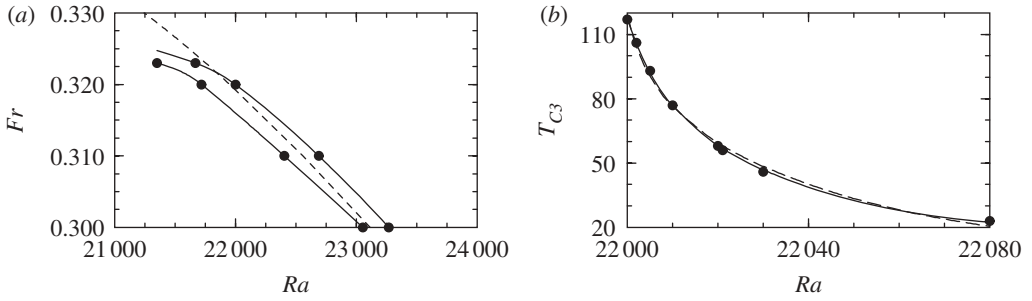

Figure 11. (*a*) SNIC bifurcation curves in (*Ra*, *Fr*) space bounding the pinning region for $\Omega = 100$, $\sigma = 7$ and $\gamma = 1$; the region is the rectangle in figure 10*b*. The dashed line is the L_u curve in the perfect case. (*b*) The period of the rotating wave C3 as it approaches the SNIC bifurcations at $Fr = 0.32$. The solid line is a cubic spline fit to the computed periods (solid symbols), and the dashed line is a square-root fit.

bifurcation of limit cycles). This curve CF originates at the Bautin point Ba. There are other flow states that are stable in this same region [25]. These additional states are well separated in phase space, and here we focus on the base state and the $m = 3$ bifurcated rotating wave.

Figure 10*c* shows the computed frequency of the limit cycle along the Hopf bifurcation curve. This frequency is negative along H_- and positive along H_+, and is zero at the ZF (zero frequency) point. At this point, we have precisely the scenario discussed in this paper: a flow (the base state) with SO(2) symmetry undergoing a Hopf bifurcation that has zero frequency at that point. Figure 10*b* also includes the line L where the frequency of the bifurcated states is zero. This curve has been computed using continuation methods, because the zero-frequency state is unstable in the lower part (L_l) of the saddle–node CF, and therefore cannot be obtained via time evolution. The zero-frequency state becomes stable upon crossing the saddle–node curve CF and moving to the upper part L_u of the saddle–node CF, and becomes observable both experimentally and by numerical simulations advancing the Navier–Stokes equations in time.

In order to break the SO(2) symmetry and see whether a pinning region appears, an imperfection has been introduced, in the form of an imposed linear temperature profile at the top lid, $\Theta(r, \theta, z = 0.5) = \epsilon\, r \cos\theta$, where ϵ is a measure of the symmetry breaking. This term completely breaks the rotational symmetry of the governing equations, and no symmetry remains. Figure 11*a* shows that the line L becomes a band of pinned solutions, steady solutions with frequency zero, as predicted by the normal form theory presented in this paper. We can also check the nature of the bifurcation taking place at the boundary of the pinning region. Figure 11*b* shows the variation of the period of the limit cycle approaching the pinning region. It is an infinite period bifurcation, and the square-root fit (shown in the figure) works better than the logarithmic fit. We estimate that the bifurcation is a SNIC bifurcation, as the normal form theory presented predicts it should be sufficiently far from the zero-frequency point ZF.

Figure 12 shows snapshots of isotherms at mid-height ($z = 0$) with $Ra = 21\,950$ and $Fr = 0.32$, which is a parameter point inside the pinning region (figure 11*a*). Figure 12*a* shows a solution in the symmetric system ($\epsilon = 0$) and figure 12*b* is the pinned solution with an imperfection of $\epsilon = 0.05$, corresponding to a maximum variation in temperature of 5 per cent ΔT at the top lid. The steady-pinned solution has broken the Z_3 symmetry; one of the three arms of the solution is closer to the wall than the other two. The attachment of the solution to the sidewall, owing to the imperfection at the top lid, results in the pinning phenomenon.

6. Summary and conclusions

The aim of this paper has been to provide a general dynamical systems description of the pinning phenomenon that is observed in systems possessing two ingredients: slowly travelling or rotating waves and imperfections. The description boils down to the unfolding of a Hopf bifurcation in

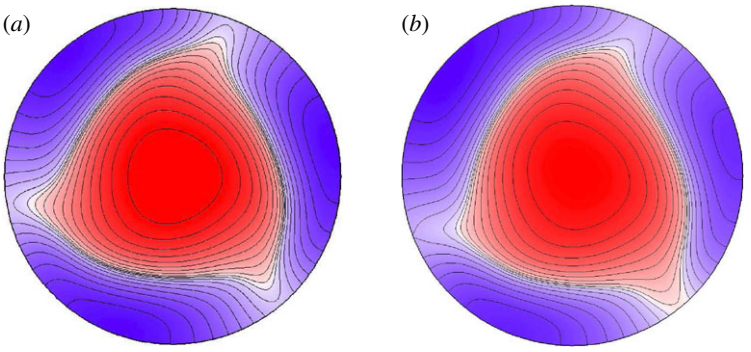

Figure 12. Isotherms at mid-height ($z = 0$) for $\Omega = 100$, $\sigma = 7$, $\gamma = 1$, $Ra = 21950$ and $Fr = 0.32$. (*a*) The symmetric solution ($\epsilon = 0$) and (*b*) a pinned solution with $\epsilon = 0.05$. There are 20 quadratically spaced contours in $T \in [-0.31, 0.31]$, with blue (red) for the cold (warm) fluid. (Online version in colour.)

an SO(2) equivariant system about the point where the Hopf frequency is zero. This turns out to be a very complicated problem owing to the degeneracies involved, but, by considering all of the low-order ways in which SO(2) symmetry may be broken near a zero-frequency Hopf bifurcation, we can identify a number of general features which are common to all scenarios, and hence can be expected to be found in practice. These are that the curve of zero-frequency splits into a region in parameter space of finite width that scales with the strength of the imperfection, and this region is delimited by SNIC bifurcations. In the very small neighbourhood of the zero-frequency Hopf bifurcation point, where the SNIC curves and the Hopf curve approach each other, the dynamics is extremely complicated, consisting in a multitude of codimension-two local bifurcations and global bifurcations. The details depend on the particulars of the imperfection, but all of these complications are very localized and are not resolvable in any practical sense. We provide two examples in canonical fluid dynamics to illustrate both the pinning phenomenon and the use of the theory to describe it. These are a Taylor–Couette flow in which the Hopf bifurcation is supercritical and a rotating Rayleigh–Bénard flow in which the Hopf bifurcation is subcritical.

This work was supported by National Science Foundation grants (nos DMS-05052705 and CBET-0608850) and Spanish Government grants (nos FIS2009-08821 and BES-2010-041542). The authors thank the referees for very useful suggestions, in particular in §4.

References

1. Golubitsky M, Schaeffer DG. 1985 *Singularities and groups in bifurcation theory*, vol. I. Berlin, Germany: Springer.
2. Golubitsky M, Stewart I, Schaeffer DG. 1988 *Singularities and groups in bifurcation theory*, vol. II. Berlin, Germany: Springer.
3. Chossat P, Iooss G. 1994 *The Couette–Taylor problem*. Berlin, Germany: Springer.
4. Golubitsky M, Stewart I. 2002 *The symmetry perspective: from equilibrium to chaos in phase space and physical space*. Basle, Switzerland: Birkhäuser.
5. Chossat P, Lauterbach R. 2000 *Methods in equivariant bifurcations and dynamical systems*. Singapore: World Scientific.
6. Crawford JD, Knobloch E. 1991 Symmetry and symmetry-breaking bifurcations in fluid dynamics. *Annu. Rev. Fluid Mech.* **23**, 341–387. (doi:10.1146/annurev.fl.23.010191.002013)
7. Keener JP. 1987 Propagation and its failure in coupled systems of discrete excitable cells. *SIAM J. Appl. Math.* **47**, 556–572. (doi:10.1137/0147038)
8. Campbell SA, Holmes P. 1992 Heteroclinic cycles and modulated travelling waves in a system with D_4 symmetry. *Physica D* **59**, 52–78. (doi:10.1016/0167-2789(92)90206-3)
9. Knobloch E, Hettel J, Dangelmayr G. 1995 Parity breaking bifurcation in inhomogeneous systems. *Phys. Rev. Lett.* **74**, 4839–4842. (doi:10.1103/PhysRevLett.74.4839)

10. Hirschberg P, Knobloch E. 1996 Complex dynamics in the Hopf bifurcation with broken translation symmetry. *Physica D* **90**, 56–78. (doi:10.1016/0167-2789(95)00227-8)
11. Dangelmayr G, Hettel J, Knobloch E. 1997 Parity-breaking bifurcation in inhomogeneous systems. *Nonlinearity* **10**, 1093. (doi:10.1088/0951-7715/10/5/006)
12. Lamb JSW, Wulff C. 2000 Pinning and locking of discrete waves. *Phys. Lett. A* **267**, 167–173. (doi:10.1016/S0375-9601(00)00097-9)
13. Westerburg M, Busse FH. 2003 Centrifugally driven convection in the rotating cylindrical annulus with modulated boundaries. *Nonlinear Proc. Geophys.* **10**, 275–280. (doi:10.5194/npg 10-275-2003)
14. Thiele U, Knobloch E. 2006 Driven drops on heterogeneous substrates: onset of sliding motion. *Phys. Rev. Lett.* **97**, 204501. (doi:10.1103/PhysRevLett.97.204501)
15. Thiele U, Knobloch E. 2006 On the depinning of a driven drop on a heterogeneous substrate. *New J. Phys.* **8**, 313. (doi:10.1088/1367-2630/8/12/313)
16. Abshagen J, Heise M, Hoffmann C, Pfister G. 2008 Direction reversal of a rotating wave in Taylor–Couette flow. *J. Fluid Mech.* **607**, 199–208. (doi:10.1017/S0022112008002176)
17. Gambaudo JM. 1985 Perturbation of a Hopf bifurcation by an external time-periodic forcing. *J. Differ. Equ.* **57**, 172–199. (doi:10.1016/0022-0396(85)90076-2)
18. Wagener F. 2001 Semi-local analysis of the k : 1 and k : 2 resonances in quasi-periodically forced systems. In *Global analysis of dynamical systems* (eds W Broer, B Krauskopf, G Vegter), p. 113. London, UK: IOP Publishing Ltd.
19. Broer H, van Dijk R, Vitolo R. 2008 Survey of strong normal-internal k : l resonances in quasi-periodically driven oscillators for l = 1, 2, 3. In *SPT 2007: Symmetry and perturbation theory: Proc. of the Int. Conf. SPT 2007 Otranto, Italy, 2–9 June 2007* (eds G Gaeta, R Vitolo, S Walcher), p. 45. Singapore: World Scientific.
20. Saleh K, Wagener FOO. 2010 Semi-global analysis of periodic and quasi-periodic normal-internal $k:1$ and $k:2$ resonances. *Nonlinearity* **23**, 2219–2252. (doi:10.1088/0951-7715/ 23/9/009)
21. Strogatz S. 1994 *Nonlinear dynamics and chaos*. London, UK: Addison-Wesley.
22. Haragus M, Iooss G. 2011 *Local bifurcations, center manifolds, and normal forms in infinite-dimensional dynamical systems*. Berlin, Germany: Springer.
23. Pacheco JR, Lopez JM, Marques F. 2011 Pinning of rotating waves to defects in finite Taylor–Couette flow. *J. Fluid Mech.* **666**, 254–272. (doi:10.1017/S0022112010004131)
24. Marques F, Mercader I, Batiste O, Lopez JM. 2007 Centrifugal effects in rotating convection: axisymmetric states and three-dimensional instabilities. *J. Fluid Mech.* **580**, 303–318. (doi:10.1017/S0022112007005447)
25. Lopez JM, Marques F. 2009 Centrifugal effects in rotating convection: nonlinear dynamics. *J. Fluid Mech.* **628**, 269–297. (doi:10.1017/S0022112009006193)
26. Kuznetsov YA. 2004 *Elements of applied bifurcation theory*, 3rd edn. Berlin, Germany: Springer.
27. Chow SN, Li C, Wang D. 1994 *Normal forms and bifurcations of planar vector fields*. Cambridge, UK: Cambridge University Press.
28. Dumortier F, Roussarie R, Sotomayor J. 1997 Bifurcations of cuspidal loops. *Nonlinearity* **10**, 1369–1408. (doi:10.1088/0951-7715/10/6/001)
29. Marques F, Meseguer A, Lopez JM, Pacheco JR, Lopez JM. 2012 Hopf bifurcation with zero frequency and imperfect SO(2) symmetry. (http://arxiv.org/abs/1206.1643)
30. Adler R. 1946 A study of locking phenomena in oscillators. *Proc. Inst. Radio Eng.* **34**, 351.
31. Pfister G, Schulz A, Lensch B. 1991 Bifurcations and a route to chaos of a one-vortex-state in Taylor–Couette flow. *Eur. J. Mech. B, Fluids* **10**, 247.
32. Marques F, Lopez JM. 2006 Onset of three-dimensional unsteady states in small-aspect ratio Taylor–Couette flow. *J. Fluid Mech.* **561**, 255–277. (doi:10.1017/S0022112006000681)
33. Pfister G, Schmidt H, Cliffe KA, Mullin T. 1988 Bifurcation phenomena in Taylor–Couette flow in a very short annulus. *J. Fluid Mech.* **191**, 1–18. (doi:10.1017/S0022112088001491)
34. Pfister G, Buzug T, Enge N. 1992 Characterization of experimental time series from Taylor–Couette flow. *Physica D* **58**, 441–454. (doi:10.1016/0167-2789(92)90130-F)
35. Mercader I, Batiste O, Alonso A. 2010 An efficient spectral code for incompressible flows in cylindrical geometries. *Comput. Fluids* **39**, 215–224. (doi:10.1016/j.compfluid.2009.08.003)
36. Sanchez J, Marques F, Lopez JM. 2002 A continuation and bifurcation technique for Navier–Stokes flows. *J. Comput. Phys.* **180**, 78. (doi:10.1006/jcph.2002.7072)
37. Mercader I, Batiste O, Alonso A. 2006 Continuation of travelling-wave solutions of the Navier–Stokes equations. *Int. J. Numer. Method Fluids* **52**, 707. (doi:10.1002/fld.1196)